Acta Biomaterialia 42 (2016) 199–208

Contents lists available at ScienceDirect

Acta Biomaterialia

journal homepage: www.elsevier.com/locate/actabiomat

Full length article

Labeling and long-term tracking of bone marrow mesenchymal stem cells *in vitro* using $NaYF_4$:Yb^{3+},Er^{3+} upconversion nanoparticles

Yufei Ma [a,b], Yuan Ji [a,b], Minli You [a,b], Shurui Wang [a,b], Yuqing Dong [a,b], Guorui Jin [a,b], Min Lin [a,b], Qiong Wang [c], Ang Li [d], Xiaohui Zhang [a,b,*], Feng Xu [a,b,*]

[a] The Key Laboratory of Biomedical Information Engineering, Ministry of Education, School of Life Science and Technology, Xi'an Jiaotong University, Xi'an 710049, PR China
[b] Bioinspired Engineering and Biomechanics Center (BEBC), Xi'an Jiaotong University, Xi'an 710049, PR China
[c] Department of Endocrinology and Metabolism, Xijing Hospital, Fourth Military Medical University, 710032 Xi'an, PR China
[d] Key Laboratory of Shaanxi Province for Craniofacial Precision Medicine Research, College of Stomatology, Xi'an Jiaotong University, Xi'an 710049, PR China

ARTICLE INFO

Article history:
Received 9 April 2016
Received in revised form 25 June 2016
Accepted 15 July 2016
Available online 17 July 2016

Keywords:
Cell tracking
Mesenchymal stem cells
Osteogenic differentiation
Upconversion nanoparticles

ABSTRACT

Mesenchymal stem cells (MSCs) hold great promise as cell therapy candidate in clinics. However, the underlying mechanisms remain elusive due to the lack of effective cell tracking approaches during therapeutic processes. In this study, we successfully synthesized and utilized $NaYF_4$:Yb^{3+},Er^{3+} upconversion nanoparticles (UCNPs) to label and track rabbit bone marrow mesenchymal stem cells (rBMSCs) during the osteogenic differentiation *in vitro*. To improve their biocompatibility and cellular uptake, we modified the UCNPs with negatively-charged poly(acrylic acid) and positively-charged poly(allylamine hydrochloride) in turns (*i.e.*, PAH-PAA-UCNPs). The effect of cellular uptake of UCNPs on the osteogenic differentiation of rBMSCs was systematically evaluated, and no significant difference was found between rBMSCs labeled with UCNPs (concentration range of 0–50 μg/mL) and UCNPs-free rBMSCs in terms of cell viability, ALP activity, osteogenic protein expressions and production of mineralized nodules. Moreover, the PAH-PAA-UCNPs at a concentration of 50 μg/mL exhibited the highest biocompatibility and stability, which could well track rBMSCs during the osteogenesis process. These results would provide a positive reference for the application of these lanthanide-doped UCNPs as fluorescent nanoprobes for stem cell tracking to further understand the mechanism of stem cell fate in tissue engineering and stem cell therapy.

Statement of Significance

Upconversion nanoparticles (UCNPs) have attracted increasing attention as alternative probes for tracking various types of cells including stem cells. The reported fluorapatite-based UCNPs with the needle-like morphology showed a little poor performance on stem cell tracking, which was possibly attributed to the low upconversion efficiency and cell labeling efficiency potentially due to nanomaterial composition, crystal structure and shape. Here, we synthesized the positively-charged $NaYF_4$:Yb^{3+},Er^{3+} UCNPs with hexagonal phase and sphere-like morphology to enhance their upconversion efficiency, biocompatibility and cellular uptake, leading to a successful tracking of rBMSCs in osteogenesis process without impairing cell viability and differentiation capacity. This study provided a necessary reference for the application of UCNPs in stem cell tracking to better understand the mechanism of stem cell fate in tissue engineering, stem cell therapy, *etc.*

1. Introduction

Mesenchymal stem cells (MSCs) are multipotent cells that can differentiate into a variety of cell types, such as adipocytes, osteoblasts and chondrocytes et al. [1–3]. Up to now, MSCs have been obtained from a range of tissues (*e.g.*, bone marrow, adipose tissue) [1] and exhibited great potentials in stem cell therapy targeting

* Corresponding authors at: The Key Laboratory of Biomedical Information Engineering, Ministry of Education, School of Life Science and Technology, Xi'an Jiaotong University, Xi'an 710049, PR China.
E-mail addresses: xiaohuizhang@mail.xjtu.edu.cn (X. Zhang), fengxu@mail.xjtu.edu.cn (F. Xu).

http://dx.doi.org/10.1016/j.actbio.2016.07.030
1742-7061/

different diseases (*e.g.*, cardiovascular disease, cancers and tissue injuries) [4]. Bone marrow mesenchymal stem cells (BMSCs), as a kind of most commonly used MSCs, have attracted much attention in clinical trials, especially for bone defect repair and bone regeneration. Indeed, accumulating evidence has proved that the transplanted BMSCs can promote bone regeneration in various animal models of bone defects through differentiation into osteoblasts [5–7]. In spite of their great potentials in stem cell therapy, the underlying mechanism remains unclear. This is mostly due to the lack of the means to find out the fate of BMSCs post transplantation [8]. Therefore, it is of great importance to track stem cells during the time scale of therapeutic process without impairing their intrinsic properties (*e.g.*, proliferation, migration and differentiation).

Various labeling techniques have been developed to track stem cell behaviors *in vitro* and *in vivo* [9–14]. Inducing report genes including green fluorescent proteins (GFPs) and luciferase has been intensively used to track and quantify cell fate, while these approaches require genetic modification of stem cells via the viral vectors for transfection [15]. A variety of exogenous probes such as quantum dots (QDs) and magnetic nanoparticles have also emerged as the effective trackers for labeling stem cells without viral transfections [16–18]. Despite all this, QDs are associated with potential issue of degradation, which may lead to fluorescence decrease and release of toxic heavy metal ions [13,14]. As for magnetic resonance imaging technique, it suffers from limited image resolution (1–3 mm^3), making it challenging to accurately detect small numbers of cells after transplantation [18]. Hence, advanced exogenous fluorescent probes with high photostability, excellent resolution and negligible side effect to stem cells are still in urgent demand.

Recently, upconversion nanoparticles (UCNPs), mostly based on lanthanide-doped nanomaterials (*e.g.*, $NaYF_4$:Yb^{3+},Er^{3+}), have attracted great interest with widespread applications in biomedicine fields [12,19–24]. Compared to conventional down-conversion fluorescent probes such as QDs and fluorescent dyes, which require ultraviolet or visible excitation wavelengthes, UCNPs exhibit high photostability, sharp emission bands, large anti-Stokes shift and deeper tissue penetration [19,25–30]. Besides, UCNPs provide minimal autofluorescence from biological tissues, which allows improved imaging sensitivity in biological systems [27,31]. Therefore, UCNPs have attracted increasing attention as alternative probes for bioimaging [32–35] and tracking various types of cells including stem cells [36–38]. For instance, fluorapatite crystals doped with Yb^{3+}/Ho^{3+} (FA:Yb^{3+}/Ho^{3+}) were used to label and track MSCs during chondrogenic differentiation [36]. However, upconversion efficiency and cell labeling efficiency of these needle-like FA:Yb^{3+}/Ho^{3+} crystals were potentially low due to their composition, crystal structure and shape, leading to a poor performance on stem cell tracking. Indeed, upconversion efficiency of FA:Yb^{3+}/Ho^{3+} crystals is relative low compared to hexagonal-phase $NaYF_4$:Yb^{3+},Er^{3+} crystals [39]. Besides, the shape and size of nanomaterial have been shown to significantly affect cellular uptake efficiency, and the nanomaterial with spherical shape has demonstrated to provide higher uptake efficiency than other shapes [40–42]. Although several studies have assessed the potential hazards of UCNPs during stem cell tracking [43,44], and these existing studies mainly focus on cytotoxicity or biocompatibility of UCNPs, the long-term effect of UCNPs on differentiation capacity and tracking of stem cells using hexagonal-phase $NaYF_4$:Yb^{3+},Er^{3+} crystals with sphere-like morphology have not been fully explored.

In this study, we synthesized $NaYF_4$:Yb^{3+},Er^{3+} UCNPs, which were then modified with poly(acrylic acid) (PAA) and poly(allylamine hydrochloride) (PAH) in sequence. Such surface modification of UCNPs is necessary to improve their water dispersibility and biocompatibility, subsequently facilitating cellular uptake [45]. Then, we used PAH-PAA-UCNPs to label New Zealand white rabbit bone marrow mesenchymal stem cells (rBMSCs), and tracked the labeled stem cells during their osteogenic differentiation *in vitro*. Cellular uptake of PAH-PAA-UCNPs and their long-term effect on osteogenic differentiation of the nanoparticle-labeled rBMSCs were systematically evaluated. This study provided the necessary data for the application of these lanthanide-based UCNPs in tracking of stem cells to further understand the mechanism of stem cell therapy, especially demonstrating their great potentials as the fluorescent cell-labeling agents in tissue engineering.

2. Materials and methods

2.1. Synthesis and characterization of PAH-PAA-UCNPs

$NaYF_4$:Yb^{3+},Er^{3+} UCNPs (Y: Yb: Er = 80:18:2) were prepared according to our recently reported protocol [46]. To make UCNPs water-soluble, a simple ligand exchange method was used to modify the surface of UCNPs. As a hydrophilic ligand, poly(acrylic acid) (PAA, Mw = 1800) was first used for replacing the original hydrophobic ligands on the surface of UNCPs by mixing 1 mL of UCNPs dispersion, 14.5 μL PAA, and 1 mL ethanol together in chloroform (15 mg/mL) with constant stirring overnight. Then the mixed solution was centrifuged at 10,000 rpm for 10 min. The precipitates were washed three times with ethanol and deionized water, then the PAA-UCNPs can be re-dispersed well in water. To reverse surface charge, poly(allylamine hydrochloride) (PAH, Mw = 17,500) was followed to modify the PAA-UCNPs, leading to a positive charge surface. 97 mg PAH, 1 mL ethanol and 1 mL PAA-UCNPs water solution were mixed overnight. After three times washing, PAH-PAA-UCNPs were obtained. The detailed process was illustrated in Fig. 1a.

Transmission electron microscopy (TEM) image was obtained by using a H7700 transmission electron microscope (acceleration voltage: 200 kV). Upconversion luminescence (UCL) emission spectra were acquired with a QuantaMasterTM40 spectrofluorometer with a 250 mW 980 nm NIR laser diode as the excitation source. X-ray powder diffraction (XRD) patterns were obtained from an XRD-7000 diffractometer over a 2θ range of 10°–80°. Zeta potential of UCNPs was analyzed by a Nano-ZS90 Zeta Sizer. Fourier transform infra-red (FT-IR) spectra were analyzed using a Nicolet iS50 FT-IR spectrometer from 4000 cm^{-1} to 400 cm^{-1}.

2.2. Rabbit bone marrow mesenchymal stem cells (rBMSCs) culture and differentiation

rBMSCs were separated from the bone shafts of femurs form New Zealand white rabbits [47]. rBMSCs were cultured in low glucose Dulbecco's modified Eagle's medium (LG-DMEM, Invitrogen) for proliferation. Growth medium (GM) contained 10% fetal bovine serum (FBS, Gibco, USA), 100 μg/mL streptomycin and 100 U/mL penicillin. 2–4th passage cells were used for different assays and cultured in an incubator (37 °C, 5% CO_2).

The prepared PAH-PAA-UCNPs were dispersed in a certain volume of growth medium to get an initial nanoparticle suspension with the concentration of 1 mg/mL. Then the initial PAH-PAA-UCNPs suspension was filtered by using a 0.22 μm membrane. Finally, the target PAH-PAA-UCNPs concentrations of 25 μg/mL, 50 μg/mL, 100 μg/mL and 200 μg/mL were obtained by adding different amounts of the filtered initial PAH-PAA-UCNPs suspension into the growth medium. The growth medium without any PAH-PAA-UCNPs was used as control in our study.

Cell pretreatment and osteogenic differentiation were shown in Fig. 1b. In brief, the rBMSCs were seeded with growth medium

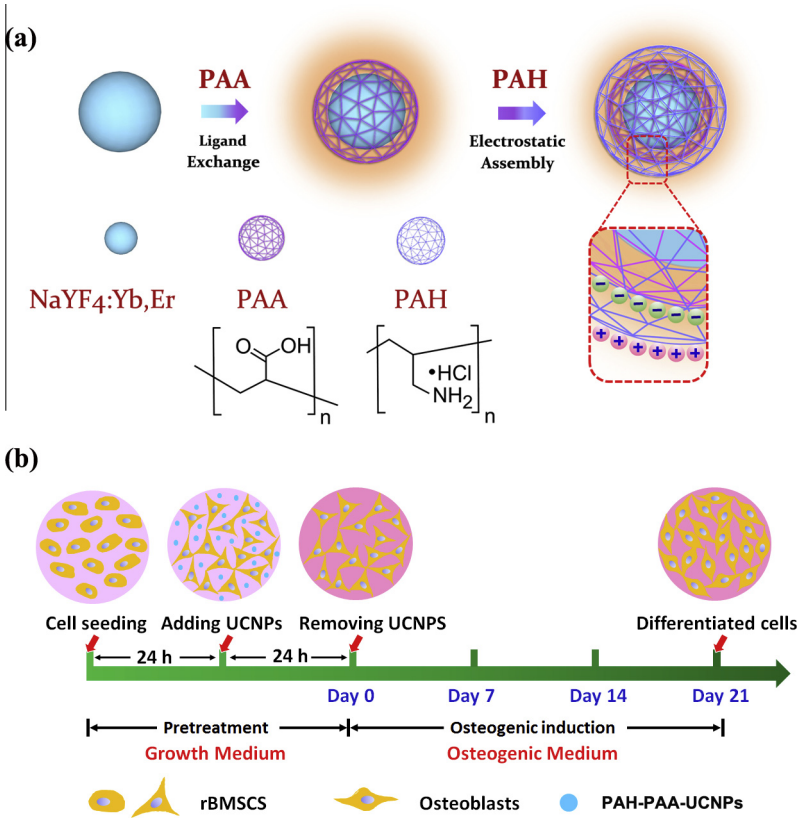

Fig. 1. Schematics of nanoparticle synthesis and process of cell pretreatment and osteogenic induction. (a) PAH-PAA-UCNPs synthesis. First, $NaYF_4$:Yb^{3+},Er^{3+} UCNPs were synthesized. Then, a ligand exchange method was used for surface modification of UCNPs. Finally, PAH was electrostatic assembled to the surface of the PAA-conjugated $NaYF_4$:Yb^{3+},Er^{3+} UCNPs, leading to the formation of PAH-PAA-UCNPs. (b) Cell pretreatment and osteogenic differentiation process. rBMSCs were exposed to the PAH-PAA-UCNPs at different concentrations for 24 h. Subsequently, osteogenic medium (OM) was used to culture cells for 21 days and the fresh medium was replaced every 3 days. Finally, the cells were taken for the different assays on the days as designed.

(GM) initially. After 1 day for cell attachment, the rBMSCs were exposed to different concentrations of PAH-PAA-UCNPs for 24 h. After that, the medium was replaced with an osteogenic medium (OM), containing 10 mM β-glycerophosphate disodium, 10^{-7} M dexamethasone and 50 μg/mL ascorbic acid. Fresh medium was replaced every 3 days. All cultures were under standard culture condition (5% CO_2, 37 °C). The rBMSCs were used for the following assays on the days as designed.

2.3. Confocal laser scanning microscopy observation for the uptake of PAH-PAA-UCNPs

The rBMSCs were seeded onto 35-mm coverglass-bottom dishes and incubated with different concentrations of PAH-PAA-UCNPs for 24 h at 37 °C. Then, the cells were rinsed with PBS three times to remove the unbound nanoparticles on cell surface. After being fixed with 4% paraformaldehyde for 15 min, the cell nuclei were stained by 4′,6-diamidino-2-phenylindole (DAPI) for 20 min at 37 °C. Cellular uptake of PAH-PAA-UCNPs was determined by a modified confocal laser scanning microscope (Olympus FV1200, Japan) equipped with an external 980-nm laser as the excitation source.

2.4. CCK-8 assay

Cell proliferation was evaluated quantitatively by using a Cell Count Kit-8 (CCK-8, 7Sea Pharmatech Co., Ltd, China). The rBMSCs were cultured at a density of 5000 cells per well in a 48-well plate. CCK-8 assays were carried out respectively on day 1 and 7 after exposure to PAH-PAA-UCNPs with different concentrations for 24 h. CCK-8 (10%, v/v) was added to the medium and then cells were incubated in it at 37 °C for 3 h. Due to the activity of dehydrogenases in living cells, CCK-8 is transformed into orange-colored formazan. 100 μL of the above solution was taken into a 96-well plate and then a microplate reader at 450 nm was used to measure the absorbance (O.D.) of the solution. O.D. at 450 nm was measured to describe the relative cells number. Then, the cell viability was expressed by normalizing the O.D. to the control (% of the control). The experiments were carried out in triplicate and three independent experiments were performed.

2.5. Flow cytometry for cell cycle analysis

The rBMSCs were cultured in a 6-well plate at an initial density of 50,000 cells per well. PAH-PAA-UCNPs were added into each well after cell seeding for 24 h, resulting in the concentrations of nanoparticle were 25, 50, 100, and 200 μg/mL. The control group was the cells without any PAH-PAA-UCNPs. After exposure to UCNPs for 24 h, the rBMSCs were rinsed with PBS and then cultured in osteogenic medium. On day 7 after osteogenic induction, the rBMSCs were harvested with trypsin-EDTA and centrifuged. After washing twice with culture medium (without FBS), 0.5 mL cell suspension was added to 1.5 mL 70% alcohol and fixed at 4 °C overnight. Then cell cycle assay was carried out by a Cell Cycle and Apoptosis Analysis Kit (7Sea Pharmatech Co., Ltd, China) according to the manufacturer's protocol, followed by measurement of fluorescence data by a flow cytometer (BD, USA). Cells in different phases of the cell cycle (*G0*/*G*1, S and *G*2/*M*) were analyzed.

2.6. Alkaline phosphatase (ALP) activity assay

The rBMSCs were seeding in 24-well plates at a density of 10,000 cells per well. After treatment with PAH-PAA-UCNPs, the cells were cultured for osteogenic differentiation. At day 7 and day 10 after osteogenic induction, the cells were rinsed and then lysed on ice using RIPA lysis buffer (HEART, China) for 15 min. Subsequently, the lysate was harvested and centrifuged at 10,000 rpm for 10 min at 4 °C and then analyzed by using an ALP Assay Kit (Jiancheng, China) based on the manufacturer's protocol. The ALP activity was normalized by the content of total protein measured by a BCA Assay Kit (Jiancheng, China).

2.7. Real-time polymerase chain reaction (RT-PCR)

The rBMSCs were seeded in a 6-well plates (cell density: 40,000 cells/well). After 14-days osteogenic induction, the total RNA for each sample was extracted by using a RNA Extraction Kit (Tiangen. Co. Ltd, China). Then the prepared RNA was reverse-transcribed with a RevertAid First Strand cDNA Synthesis Kit (Thermo Scientific, USA) on the basis of the suggested protocol. RT-PCR analysis was performed by using a real-time PCR system (ABI 7500 Fast, USA) with SYBR Green PCR Master Mix (Life Technologies, USA). Runx 2, osteopontin (OPN) and osteocalcin (OC) were used to assess the osteogenic differentiation and GAPDH served as a housekeeping gene. The sense and antisense primers in the present study were designed and shown in Table 1. The experiments were performed in triplicate.

Table 1
Sequences of primers for RT-PCR.

Gene	Forward primer (5′-3′)	Reverse primer (5′-3′)
GAPDH	AGGTCGGTGTGAACGGATTTG	TGTAGACCATGTAGTTGAGGTCA
Runx 2	CACTATCCAGCCACCTTTACTT	TGGCAGGTAGGTATGGTAGT
OPN	CGAGCAGGCCAGACAATATAA	GATTCCTGGCTGACTTTGGA
OC	CACAGAGCGACAGCATGAG	CTTGGACACGAAGGCTGAG

2.8. Alizarin red S staining for accumulated calcium

The rBMSCs were seeded in 24-well plates at a density of 10,000 cells per well. After 21-days osteo-induction, the cells were washed, fixed with 4% paraformaldehyde for 20 min, and then stained with Alizarin Red S solution (HEART, China) at 37 °C for 20 min. Following washing the rBMSCs with PBS three times, a phase-contrast microscope (Leica, Germany) was used to photograph. To further quantify retention of Alizarin Red, the stained rBMSCs were reacted with 500 μL of 10 (w/v%) cetylpyridinium chloride in disodium hydrogen phosphate at 37 °C for 10 min, then the O.D. was measured via microplate reader at 570 nm.

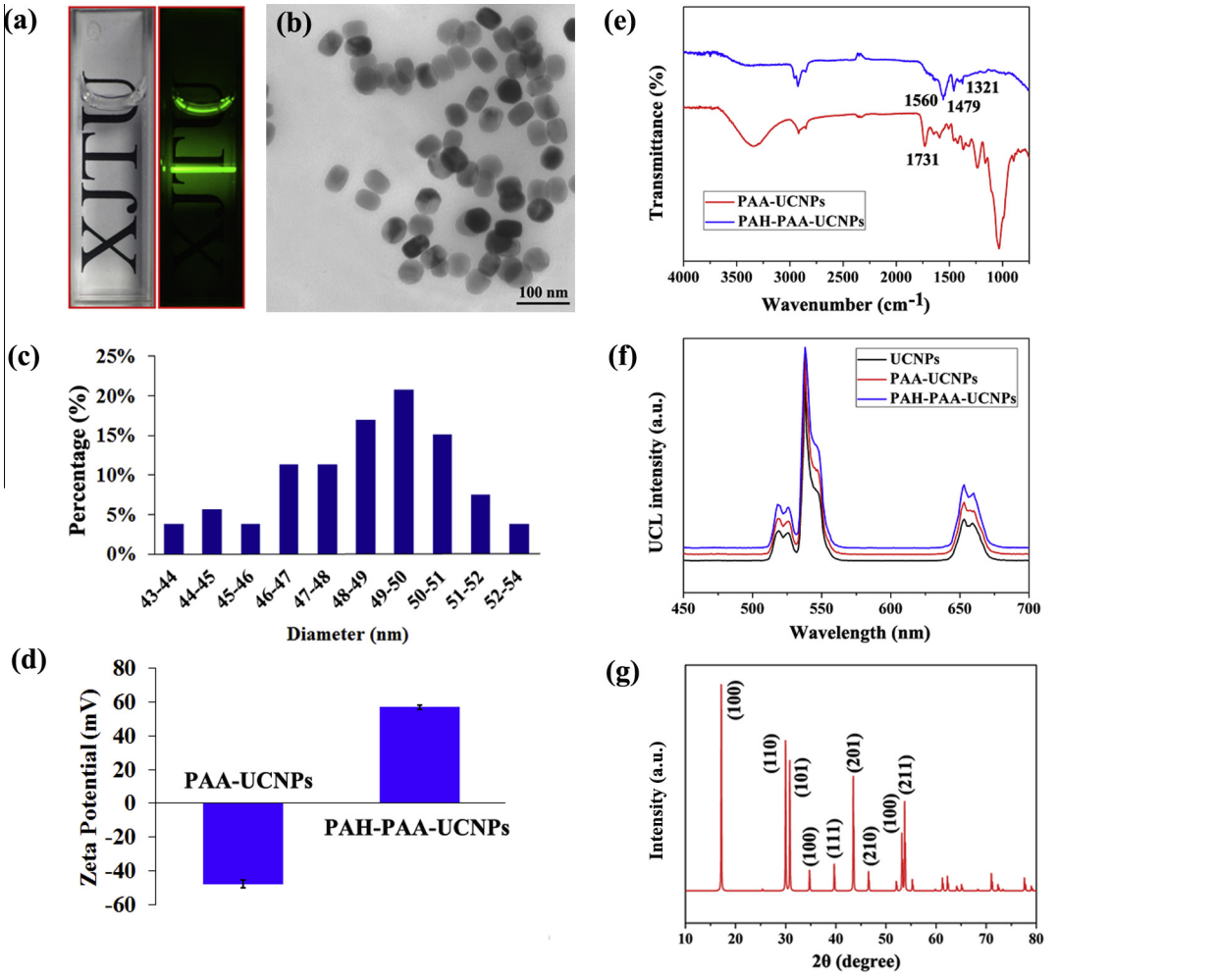

Fig. 2. Characterization of UCNPs. (a) Photos of PAH-PAA-UCNPs in PBS buffer under a 980-nm laser excitation and the ambient light. (b) Representative TEM image, (c) Size distribution and (d) Zeta potential of synthesized PAH-PAA-UCNPs. (e) FT-IR spectra of PAA-UCNPs and PAH-PAA-UCNPs (f) Upconversion luminescence emission spectrum of three kinds of UCNPs. (f) XRD patterns of PAH-PAA-UCNPs after hydrothermal synthesis. Scale bar: 100 μm.

2.9. In vitro tracking of rBMSCs during osteogenesis process

The rBMSCs were seeded onto 35-mm coverglass-bottom dishes first, and then exposed to the PAH-PAA-UCNPs with the concentration of 50 μg/mL. After that, the cells were cultured in osteogenic medium. *In vitro* tracking of rBMSCs during osteogenesis process using PAH-PAA-UCNPs was studied by immunofluorescent assay at day 5, day 14 and day 21 after osteo-induction. Immunofluorescent staining analysis of OC was carried out by incubating the rBMSCs with the mouse anti-OC antibody (1:200, ab13418, abcam) overnight at 4 °C. Next, the rBMSCs were labeled with the anti-mouse secondary antibody (Rhodamine, 1:1000, Jackson-Yeasen). The nuclei were stained with DAPI for 10 min at room temperature. The images were visualized and photographed under a modified confocal laser scanning microscope.

2.10. Statistical analysis

Experimental results are presented as means ± standard deviation (S.D.). Comparisons between groups were analyzed by ANOVA using SPSS. Differences were accepted to be statistical significance at a level of $p < 0.01$.

3. Results and discussion

3.1. Characterization of PAH-PAA-UCNPs

To obtain the fluorescent nanoprobes for cell labeling with enhanced cellular uptake, we first synthesized $NaYF_4$:Yb^{3+},Er^{3+} UCNPs and then modified UCNPs with PAA and PAH via ligand exchange and electrostatic assembly in sequence (*i.e.*, PAH-PAA-UCNPs). PAH-PAA-UCNPs formed a clear and highly stable solution in PBS. When excited with a 980 nm NIR laser diode, we observed strong upconversion luminescence from PAH-PAA-UCNPs dispersed in PBS with naked eyes (Fig. 2a). The representative TEM image shows the monodispersed and sphere-like nanoparticles with an average diameter about 50 nm (Fig. 2b-c). Coating UCNPs with positive charge has been demonstrated to enhance their cellular uptake, which could be attributed to the negative charge of cell surface [37]. In the present study, the modified UCNPs have positive charge, as reflected by the Zeta potential of PAH-PAA-UCNPs (+56.8 mV) as compared to PAA-UCNPs (–47.8 mV) (Fig. 2d). The size distribution of UCNPs based on dynamic light scattering (DLS) technique was investigated to reveal the change of size distribution after surface modification (Fig. S1). We observed that the hydrodynamic diameter of UCNPs increased after PAA and PAH modification, respectively. Besides, the successful modification of UCNPs with PAA and PAH coating was also confirmed by FT-IR (Fig. 2e). The transmission band at 1731 cm^{-1} is attributed to the –COOH on the surface of PAA-UCNPs. While the bands at 1560 cm^{-1} and 1479 cm^{-1} can be assigned to amide II, and the band at 1321 cm^{-1} is attributed to amide III, indicating the existence of PAH coating [48]. The upconversion luminescence spectrum of UCNPs and the surface modified UCNPs were determined by using a 980 nm laser as the excitation source, revealing the typical upconversion luminescence peaks of Er^{3+} doped UCNPs around 540 nm and 650 nm, whether the surface modification or not (Fig. 2f). Finally, XRD patterns of synthesized PAH-PAA-UCNPs were analyzed (Fig. 2g). We observed that all sharp diffraction peaks at approximately 17.1°, 29.9°, 30.8°, 34.7°, 39.8°, 43.5°, 46.5°, 53.1° and 53.7° corresponds well to (1 0 0), (1 1 0), (1 0 1), (1 0 0), (1 1 1), (2 0 1), (2 1 0), (1 0 0) and (2 1 1) lattice planes of the typical hexagonal phase of β-$NaYF_4$ (JCPDS 16-0334).

3.2. Determination of cellular uptake of UCNPs

To determine the cellular uptake of PAH-PAA-UCNPs, we exposed the rBMSCs to varied concentrations of PAH-PAA-UCNPs

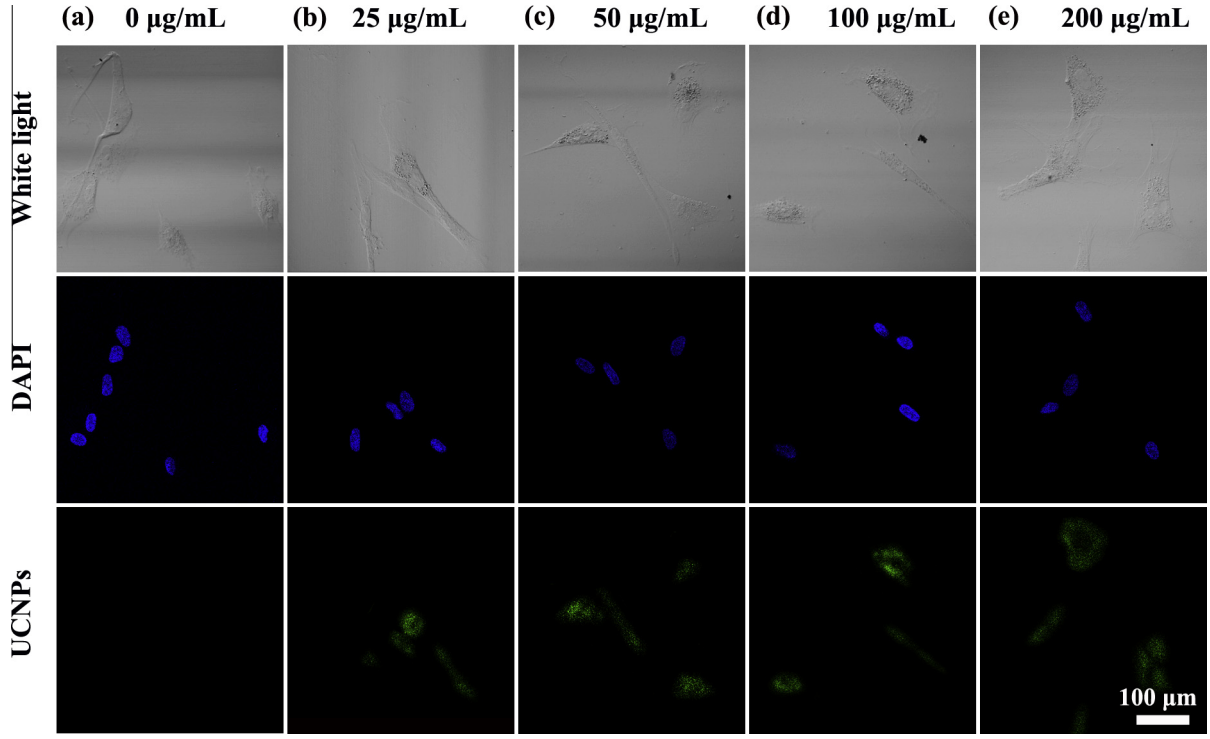

Fig. 3. Uptake of PAH-PAA-UCNPs into rBMSCs. Confocal laser scanning microscopy images of rBMSCs after treatment with PAH-PAA-UCNPs (excited by 980 nm light) at concentration of (a) 0, (b) 25, (c) 50, (d) 100 and (e) 200 μg/mL for 24 h. All images were taken under the identical instrumental condition and presented at the same intensity scale. Blue and green colors represent blue fluorescence and upconversion luminescence signals form DAPI (nucleus staining) and PAH-PAA-UCNPs, respectively. Scale bar: 100 μm. (For interpretation of the references to color in this figure legend, the reader is referred to the web version of this article.)

(0, 25, 50, 100 and 200 μg/mL) for 24 h and imaged the cells using a confocal laser scanning microscopy with 980 nm exciting light source (Fig. 3). We observed upconversion luminescence from all rBMSCs exposed to PAH-PAA-UCNPs and quantified the uptake of UCNPs in terms of fluorescence intensity (as fluorescent area per cell). The fluorescence intensity increased with increasing nanoparticle concentrations ranging from 25 μg/mL to 200 μg/mL (Fig. 3b-e and Fig. S2), indicating a dose-dependent uptake. No fluorescence in the control group (*i.e.*, cells incubated without any nanoparticle) was observed (Fig. 3a). This result indicates that the rBMSCs were efficiently labeled with PAH-PAA-UCNPs. Also from the fluorescent images, we found that the nanoparticles were mainly located at the cytoplasmic and the perinuclear regions, which is consistent to the results reported in literature [37]. Wang et al. studied the cellular uptake mechanism and believed that the cellular uptake of UCNPs could likely via the energy dependent endocytosis [37].

3.3. Cell viability and cell cycle

To assess the effect of nanoparticle labeling on cell proliferation, rBMSCs were exposed to PAH-PAA-UCNPs for 24 h and then cultured in osteogenic medium for further osteogenic differentiation. We observed that cell number increased from day 1 to day 7 in all groups (Fig. 4a). Besides, cell viability at day 1 decreased with increasing nanoparticle concentration, indicating the potential cytotoxic effect of PAH-PAA-UCNPs. For instance, the dose-dependent cell viabilities at day 1 were 85 ± 8%, 77 ± 7%, 56 ± 5% and 44 ± 2% respectively. At day 7, cell viability decreased significantly only at the concentration of 100 μg/mL and 200 μg/mL ($p < 0.01$) (Fig. 4b), indicating a negligible cytotoxic effect of PAH-PAA-UCNPs when the concentration is less than 50 μg/mL. Additionally, when the concentration increased to 200 μg/mL, cell viability on day 7 decreased sharply to 25 ± 6%, even lower than that on day 1, indicating a strong cytotoxicity of PAH-PAA-UCNPs at 200 μg/mL.

To further study the effect of PAH-PAA-UCNPs uptake on cell proliferation, we analyzed cell cycle of rBMSCs by performing DNA staining with propidium iodide after 7 days of osteogenic induction (Fig. 4c). The percentage of DNA synthesis (*S*) phase + gap 2/mitosis phase (*G2*/*M*) in cell cycle could be reflected the effect of PAH-PAA-UCNPs on rBMSCs proliferation. We observed that the percentage of nanoparticle-treated rBMSCs in *G0*/*G1* phase increased significantly ($p < 0.01$) than that in control group, while the percentage of *S* + *G2*/*M* phase of rBMSCs decreased significantly ($p < 0.01$) at the concentration of 100 and 200 μg/mL. It indicates that PAH-PAA-UCNPs do affect cell proliferation of rBMSCs when exposed to high nanoparticle concentration (*e.g.*, 100 and 200 μg/mL), agreeing with the cell viability results.

Previous studies have reported that PAH was commonly used as a surface modifier of nanoparticles to improve their hydrophilicity and biocompatibility [49,50]. Moreover, PAH as a positively-charged polyelectrolyte to coat the surface of nanoparticles can efficiently enhance the cellular uptake of nanoparticles due to the negative charge of cell surface [51]. It was revealed that the cytotoxicity of nanoparticles relied on the concentration for different cell lines [43]. For example, Wang et al. [52] reported the influence of PAH-coated gold nanoparticles with the different treatment doses and found that higher treatment doses induced higher cytotoxicity. In the present work, cell viabilities at day 1 decreased with increasing PAH-PAA-UCNPs concentration, indicating a does-dependent cytotoxicity, which was consistent with the previous studies. Although the cytotoxicity of UCNPs depends on their concentration, the mechanisms of UCNP-induced cytotoxicity are still debatable. It is known that many of the nanomaterials may induce oxidative stress to cells by producing reactive oxygen species (ROS), which can damage proteins, DNA and lipids, leading to a high degree of cytotoxicity [53]. However, some other researchers used a dihydroethidium (DHE) probe to assess intracellular peroxide and superoxide levels in MSCs and their results demonstrated that DHE levels were not significantly higher in UCNPs treated groups compared to control, indicating little ROS generation was induced by cellular uptake of UCNPs [37]. One possible mechanism of toxicity was proposed by Zhang et al. [44], which suggested that the releasing of metal ions and ligands from UCNPs was responsible for cytotoxicity. Despite all this, most studies only focused on acute cytotoxicity and investigated cell viability within 48 h. For the differentiation of rBMSCs, the long-lasting effect of UCNPs on cell viability should also be taken into consideration during a long differentiation process. Our results showed that after 7 days of osteogenic induction, the PAH-PAA-UCNPs showed negligible cytotoxicity to rBMSCs with concentrations of less than

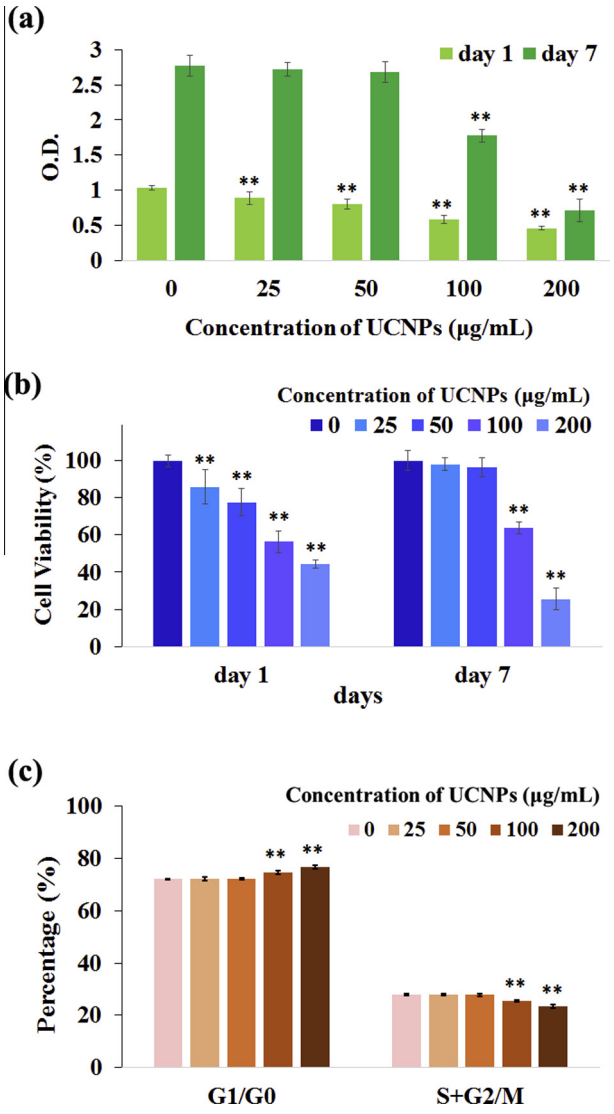

Fig. 4. Relative cells number (a), cell viability (b) determined by CCK-8 and cell cycle (c) analyzed by flow cytometer. The rBMSCs were exposed to different concentration of PAH-PAA-UCNPs (0, 25, 50, 100 and 200 μg/mL) for 24 h, then the cells were cultured in osteogenic medium. CCK-8 tests were carried out at day 1 and day 7 after osteo-induction, while cell cycle analyses were conducted at day 7. Data was expressed as mean ± SD. (n = 5 for each sample). Double asterisks (**) denote statistical significance $p < 0.01$ compared with control group (concentration of PAH-PAA-UCNPs: 0 μg/mL).

50 μg/mL. Even though cell viability decreased as a function of nanoaprticle concentration, it did not hit below 50% at the concentration of 100 μg/mL. Therefore, the synthesized PAH-PAA-UCNPs showed no long-term cytotoxic effect on the rBMSCs within the reasonable concentrations.

3.4. Cell differentiation

To investigate the osteogenic differentiation of rBMSCs labeled with PAH-PAA-UCNPs, we assessed alkaline phosphatase (ALP) activity, the expression of Runx 2, OPN (osteopontin) and OC (osteocalcin), Fig. 5. We studied the normalized ALP activity of the labeled rBMSCs after 7 and 10 days of osteo-induction and observed no significant differences ($p > 0.05$) in ALP activity between groups treated with different nanoparticle concentration either at day 7 or day 10, but ALP activity at day 10 was higher than that at day 7 (Fig. 5a). It suggests that there is no significant influence of PAH-PAA-UCNPs on the ALP activity of rBMSCs in the tested range of nanoparticle concentrations.

We further analyzed the expressions of osteogenesis relative proteins (*i.e.*, Runx 2, OPN and OC) in rBMSCs treated with PAH-PAA-UCNPs for 14 days by using RT-PCR (Fig. 5b). For Runx 2 and OC, the relative mRNA expression result revealed that there was no significant difference ($p > 0.05$) in the groups treated with PAH-PAA-UCNPs at concentrations of 25, 50 and 100 μg/mL compared with control group. When the concentration of PAH-PAA-UCNPs increased to 200 μg/mL, the mRNA expression levels decreased significantly ($p < 0.01$). The relative mRNA expression level of OPN was significantly lower ($p < 0.01$) in rBMSCs exposed to PAH-PAA-UCNPs at concentration of 100 and 200 μg/mL compared with control group. All these results indicate that the osteogenic differentiation capacity of rBMSCs could not be affected by the exposed PAH-PAA-UCNPs at reasonable concentration (<50 μg/mL).

Production of the mineralized nodules is an important indicator for osteogenic differentiation [54]. To further investigate the effect of PAH-PAA-UCNPs on osteogenic differentiation of the labeled rBMSCs, we stained the cells with Alizarin Red S after 21 days of osteo-induction (Fig. 6a–e). We observed the orange-red precipitates in all groups, indicating that the labeled rBMSCs could maintain the capability of osteogenic differentiation. To quantify the effect of nanoparticle concentration on osteogenic differentiation, we measured the precipitated orange-red nodules in terms of O. D. at 570 nm and found that the production of the mineralized nodules in the groups of 100 μg/mL and 200 μg/mL was significantly lower compared to the control group (Fig. 6f). This result suggests that the UCNPs-labeled rBMSCs in certain range of concentrations show little difference in osteogenic differentiation capacity, which is consistent with the PCR results.

To investigate whether PAH-PAA-UCNPs can be used to track rBMSCs during their osteogenesis process, rBMSCs were exposed to PAH-PAA-UCNPs at concentration of 50 μg/mL based on the above results, and then induced in the osteogenic differentiation medium for 21 days. Cells were tracked at day 5, day 14 and day 21 via confocal microscopy (Fig. 7). OC, as a typical protein synthesized only by osteoblast, was detected by immunofluorescent assay to determine whether osteogenic differentiation occurred or not. We found that rBMSCs were positive to OC after 14 days of osteoinduction, and OC expression increased gradually with incubation time, while strong upconversion fluorescence was always observed in the labeled rBMSCs during the whole process of osteogenic differentiation. These results indicate that

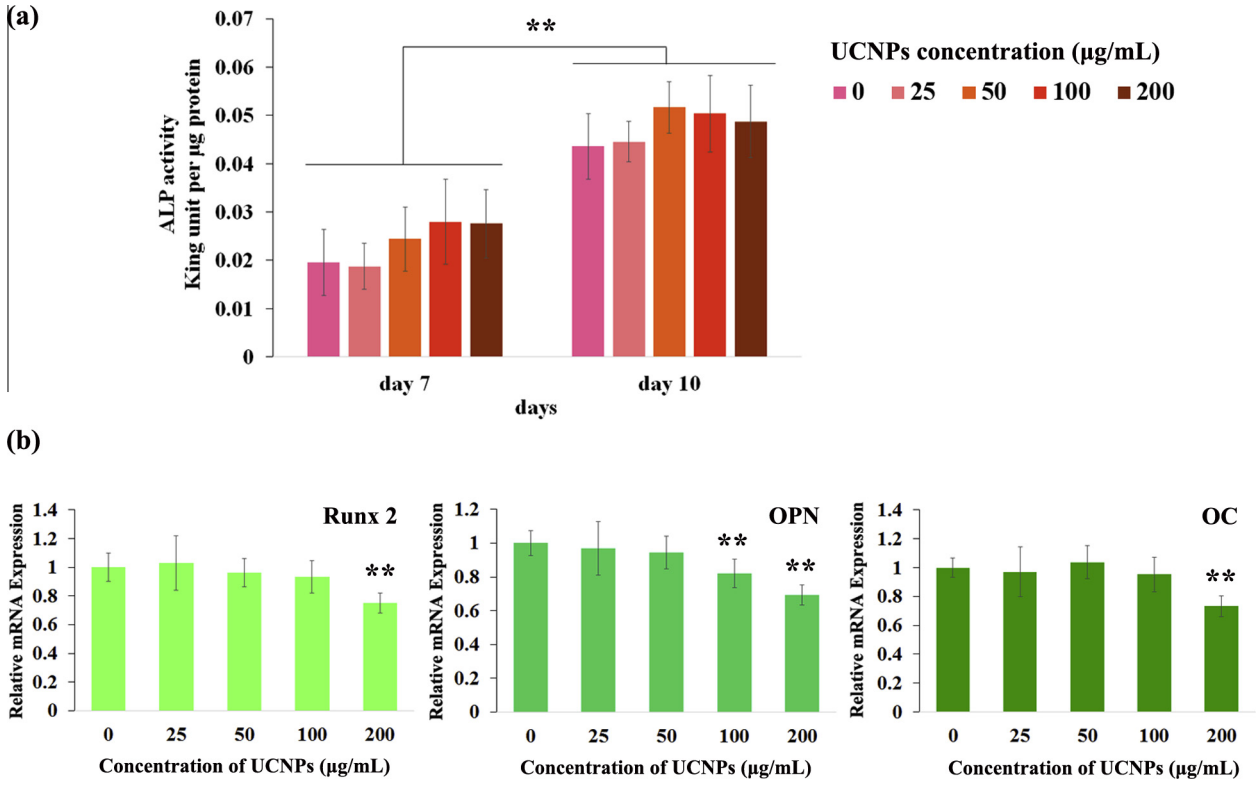

Fig. 5. *In vitro* osteogenic differentiation capacity of rBMSCs after exposure to PAH-PAA-UCNPs with different concentrations. (a) Normalized alkaline phosphatase activity expression by rBMSCs. After treatment with PAH-PAA-UCNPs (0, 25, 50, 100 and 200 μg/mL) for 24 h, the rBMSCs were cultured in the osteogenic medium and ALP activity was analyzed at day 7 and 10 after osteogenic induction. Data was expressed as mean ± SD. (n = 5 for each sample). No significant differences ($p > 0.05$) are found either at day 7 or day 10. (b) The influence of PAH-PAA-UCNPs treatment on osteogenic genes expression. Real-time PCR was performed with rBMSCs treated as in (a) at day 14 after osteo-induction to analyze the expression of Runx 2, OPN and OC. Each bar represents mean ± SD from three independent experiments, and each performed in triplicate. Double asterisks (**) denote statistical significance $p < 0.01$ compared with control group (concentration of PAH-PAA-UCNPs: 0 μg/mL).

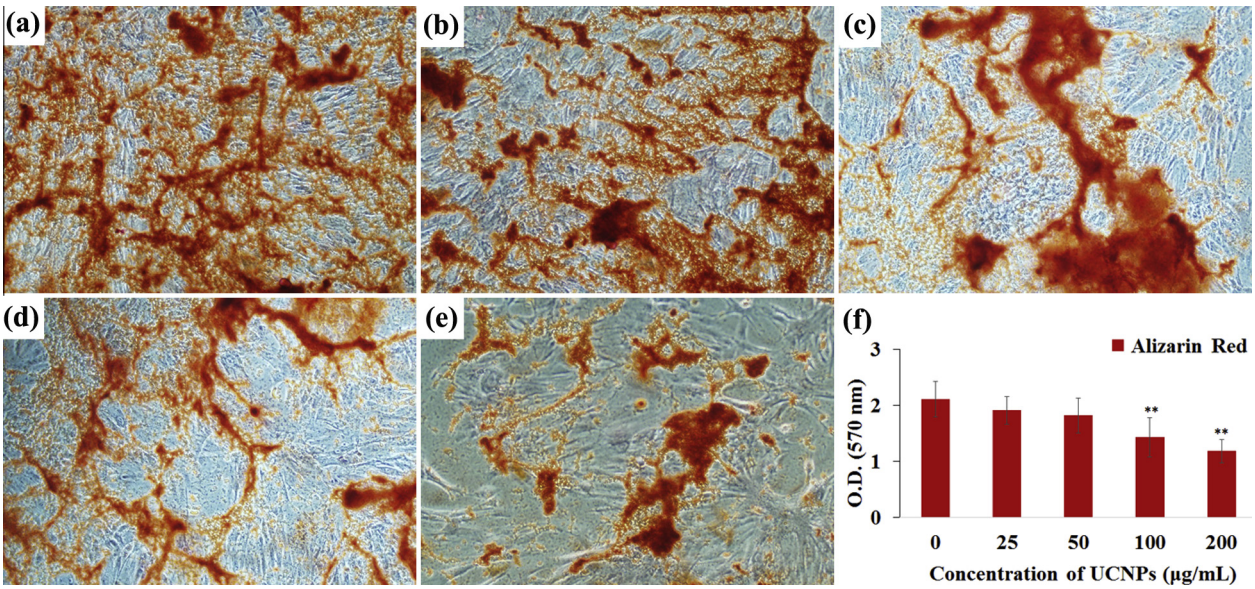

Fig. 6. Alizarin red S staining for mineralized nodular structures for osteogenesis. (a) 0, (b) 25, (c) 50, (d) 100 and (e) 200 μg/mL PAH-PAA-UCNPs were added to the rBMSCs for 24 h and then the osteogenic medium was used. Alizarin red S was conducted at day 21 after osteo-induction. (f) The quantitative result of retention of Alizarin red S. Data were expressed as means ± SD (n = 3 for each sample). Double asterisks (**) denote statistical significance $p < 0.01$ compared to data obtained from the control. (For interpretation of the references to color in this figure legend, the reader is referred to the web version of this article.)

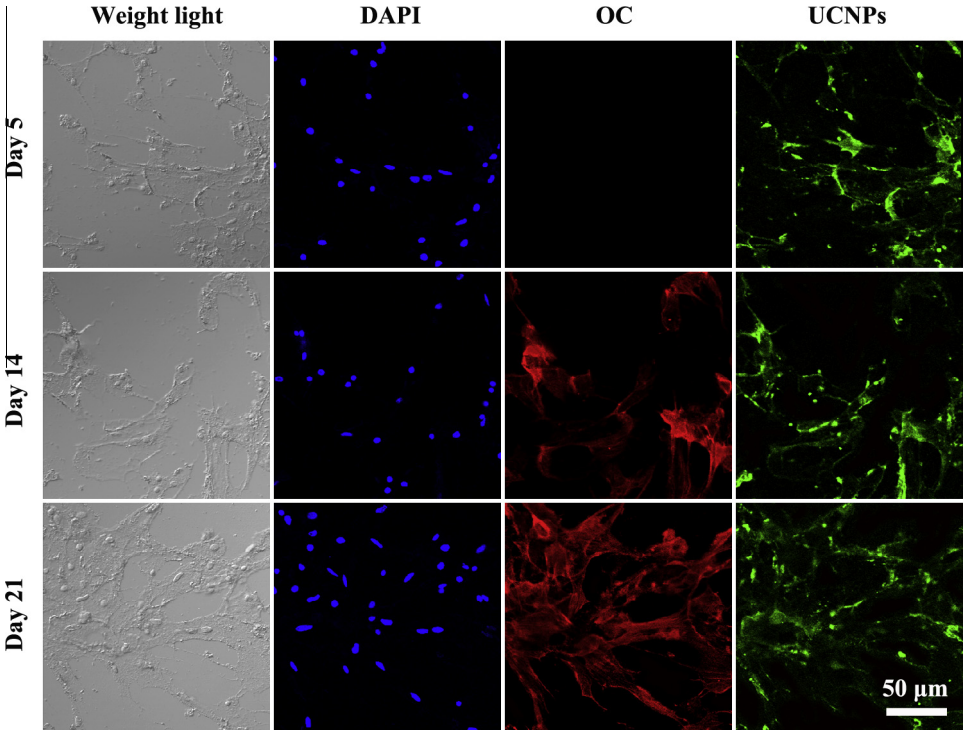

Fig. 7. *In vitro* tracking of rBMSCs during osteogenic differentiation using PAH-PAA-UCNPs. The cultured rBMSCs were treated with 50 μg/mL PAH-PAA-UCNPs first, and then induced by osteogenic differentiation medium for 21 days. Osteogenic differentiation was analyzed by immunofluorescent staining method. Confocal laser scanning microscopy images of rBMSCs were taken after 5 days, 14 days and 21 days of osteoinduciton. Blue color: nucleus staining. Red color: immunofluorescent staining for OC. Green color: upconversion luminescence signals from PAH-PAA-UCNPs. Scale bar: 50 μm. (For interpretation of the references to color in this figure legend, the reader is referred to the web version of this article.)

PAH-PAA-UCNPs can be used to track the osteogenesis process of rBMSCs *in vitro*.

Stem cells have found widespread applications in tissue engineering and regenerative medicine, where the fate of the transplanted stem cells remains unclear. Therefore, we reported the application of recently developed UCNPs to label and track stem cells. To address this challenge, UCNPs need to remain in stem cells without exocytosis during a long-term tracking period. Indeed, various factors including cell type, physicochemical properties of nanoparticles, nanoparticles concentration, cellular incubation

time and distribution of nanoparticles into organelles have been shown to affect the exocytosis of nanoparticles [55]. Previously, studies have confirmed that the internalized UCNPs within MSCs did not leak out via exocytosis for 10-day and 14-day periods, respectively [37,56]. In our study, PAH-PAA-UCNPs could stay within the rBMSCs for 21 days after cellular uptake, which was in agreement with previous observations. In the present work, the natural acidification within the endosome may protonate PAH on the surface of the internalized PAH-PAA-UCNPs, inducing chloride ion influx, osmotic swelling and then destabilization of the vesicle, leading to release of PAH-PAA-UCNPs into the cytoplasm [57]. Stayton et al. [58] showed that nanoparticles that leave the vesicles or lysosomes and translocate into the cytoplasm have greater difficulty in exocytosis. Additionally, the prolonged pre-incubation time (24 h) in our study could also be responsible for the extension of the intracellular nanoparticles retention [55]. During a 24 h incubation with PAH-PAA-UCNPs, nanoparticles probably had more chance to be transported to the slow recycling compartments, leading to a lower exocytosis rate [55,59]. Besides, it was also required that the nanoparticles could be biocompatible without impairing the differentiation capacity of stem cell. Herein, we then investigated the influence of PAH-PAA-UCNPs on osteogenic differentiation of the labeled rBMSCs. Osteogenic differentiation capacity of the labeled rBMSCs was found to be independent of PAH-PAA-UCNPs in the certain range of concentration (0–50 μg/mL), as reflected at protein level (ALP activity), gene level (expression of proteins related with the osteogenesis, *e.g.*, Runx 2, OPN and OC) and the formation of the mineralized nodules. Although cell viabilities at day 1 decreased with increasing nanoparticle concentration, a 24 h incubation with 50 μg/mL PAH-PAA-UCNPs showed good biocompatibility, which could effectively label rBMSCs and then successfully track them in their osteogenesis process *in vitro*. Furthermore, although the rBMSCs labeled with PAH-PAA-UCNPs at concentrations of less than 50 μg/mL exhibited similar differentiation capacity as the unlabeled control group, *in vivo* study is needed in future.

4. Conclusion

In summary, we prepared upconversion nanoparticles for cell labeling and then tracked rBMSCs in the osteogenesis process *in vitro*. The modified $NaYF_4$:Yb^{3+},Er^{3+} UCNPs with positive charge using PAA and PAH (*i.e.*, PAH-PAA-UCNPs) were synthesized to enhance their biocompatibility and cellular uptake, leading to the improved cell labeling efficiency. We systematically studied the long-term effect of PAH-PAA-UCNPs on the labeled rBMSCs during the osteogenic differentiation process and found no significant difference in cell viability and differentiation capacity in a certain range of nanoparticle concentrations (0–50 μg/mL). Additionally, PAH-PAA-UCNPs at concentration of 50 μg/mL showed a great performance in biocompatibility and stability that could track rBMSCs in the osteogenesis process. Hence, these surface modified $NaYF_4$:Yb^{3+},Er^{3+} UCNPs held great potentials as fluorescent nanoprobes for stem cell labeling and tracking to better understand the mechanism of stem cell fate in tissue engineering, stem cell therapy, *etc.*

Conflicts of interest

The authors confirm that there is no conflict of interest.

Acknowledgement

This work was supported by the National Natural Science Foundation of China (51502238, 11532009, 11372243, 11522219), China Postdoctoral Science Foundation (2015M572569), Natural Science Foundation of Shaanxi Province of China (2014JM4195) and the Fundamental Research Funds for the Central Universities (xjj2015052).

Appendix A. Supplementary data

Supplementary data associated with this article can be found, in the online version, at http://dx.doi.org/10.1016/j.actbio.2016.07.030.

References

[1] M.F. Pittenger, A.M. Mackay, S.C. Beck, R.K. Jaiswal, R. Douglas, J.D. Mosca, M.A. Moorman, D.W. Simonetti, S. Craig, D.R. Marshak, Multilineage potential of adult human mesenchymal stem cells, Science 284 (1999) 143–147.
[2] Y.H. Jiang, B.N. Jahagirdar, R.L. Reinhardt, R.E. Schwartz, C.D. Keene, X.R. Ortiz-Gonzalez, M. Reyes, T. Lenvik, T. Lund, M. Blackstad, J.B. Du, S. Aldrich, A. Lisberg, W.C. Low, D.A. Largaespada, C.M. Verfaillie, Pluripotency of mesenchymal stem cells derived from adult marrow, Nature 418 (2002) 41–49.
[3] S. Mendez-Ferrer, T.V. Michurina, F. Ferraro, A.R. Mazloom, B.D. MacArthur, S. A. Lira, D.T. Scadden, A. Ma'ayan, G.N. Enikolopov, P.S. Frenette, Mesenchymal and haematopoietic stem cells form a unique bone marrow niche, Nature 466 (2010) U829–U859.
[4] C. Ren, S. Kumar, D. Chanda, J. Chen, J.D. Mountz, S. Ponnazhagan, Therapeutic potential of mesenchymal stem cells producing interferon-α in a mouse melanoma lung metastasis model, Stem Cells 26 (2008) 2332–2338.
[5] L. Qin, D. Yao, L.Z. Zheng, W.C. Liu, Z. Liu, M. Lei, L. Huang, X.H. Xie, X.L. Wang, Y. Chen, X.S. Yao, J. Peng, H. Gong, J.F. Griffith, Y.P. Huang, Y.P. Zheng, J.Q. Feng, Y. Liu, S.H. Chen, D.M. Xiao, D.P. Wang, J.Y. Xiong, D.Q. Pei, P. Zhang, X.H. Pan, X. H. Wang, K.M. Lee, C.Y. Cheng, Phytomolecule icaritin incorporated PLGA/TCP scaffold for steroid-associated osteonecrosis: proof-of-concept for prevention of hip joint collapse in bipedal emus and mechanistic study in quadrupedal rabbits, Biomaterials 59 (2015) 125–143.
[6] Z.W. Ren, Y. Wang, S.Q. Ma, S. Duan, X.P. Yang, P. Gao, X. Zhang, Q. Cai, Effective bone regeneration using thermosensitive poly(N-Isopropylacrylamide) grafted gelatin as injectable carrier for bone mesenchymal stem cells, ACS Appl. Mater. Interfaces 7 (2015) 19006–19015.
[7] Z.X. Wang, C. Chen, Q. Zhou, X.S. Wang, G.D. Zhou, W. Liu, Z.Y. Zhang, Y.L. Cao, W.J. Zhang, The treatment efficacy of bone tissue engineering strategy for repairing segmental bone defects under osteoporotic conditions, Tissue Eng. Part A 21 (2015) 2346–2355.
[8] K. Andreas, R. Georgieva, M. Ladwig, S. Mueller, M. Notter, M. Sittinger, J. Ringe, Highly efficient magnetic stem cell labeling with citrate-coated superparamagnetic iron oxide nanoparticles for MRI tracking, Biomaterials 33 (2012) 4515–4525.
[9] H. Hama, H. Kurokawa, H. Kawano, R. Ando, T. Shimogori, H. Noda, K. Fukami, A. Sakaue-Sawano, A. Miyawaki, Scale: a chemical approach for fluorescence imaging and reconstruction of transparent mouse brain, Nat. Neurosci. 14 (2011). 1481-U1166..
[10] M.E. Tanenbaum, L.A. Gilbert, L.S. Qi, J.S. Weissman, R.D. Vale, A protein-tagging system for signal amplification in gene expression and fluorescence imaging, Cell 159 (2014) 635–646.
[11] N.M. Idris, Z.Q. Li, L. Ye, E.K.W. Sim, R. Mahendran, P.C.L. Ho, Y. Zhang, Tracking transplanted cells in live animal using upconversion fluorescent nanoparticles, Biomaterials 30 (2009) 5104–5113.
[12] G. Tian, Z.J. Gu, L.J. Zhou, W.Y. Yin, X.X. Liu, L. Yan, S. Jin, W.L. Ren, G.M. Xing, S. J. Li, Y.L. Zhao, Mn^{2+} dopant-controlled synthesis of NaYF4:Yb/Er upconversion nanoparticles for in vivo imaging and drug delivery, Adv. Mater. 24 (2012) 1226–1231.
[13] D.R. Larson, W.R. Zipfel, R.M. Williams, S.W. Clark, M.P. Bruchez, F.W. Wise, W. W. Webb, Water-soluble quantum dots for multiphoton fluorescence imaging in vivo, Science 300 (2003) 1434–1436.
[14] S.H. Nam, Y.M. Bae, Y.I. Park, J.H. Kim, H.M. Kim, J.S. Choi, K.T. Lee, T. Hyeon, Y. D. Suh, Long-term real-time tracking of lanthanide ion doped upconverting nanoparticles in living cells, Angew. Chem. Int. E.d. 50 (2011) 6093–6097.
[15] H. Wang, F. Cao, A. De, Y. Cao, C. Contag, S.S. Gambhir, J.C. Wu, X.Y. Chen, Trafficking mesenchymal stem cell engraftment and differentiation in tumor-bearing mice by bioluminescence imaging, Stem Cells 27 (2009) 1548–1558.
[16] L.S. Shah, P.A. Clark, E.K. Moioli, M.A. Stroscio, J.J. Mao, Labeling of mesenchymal stem cells by bioconjugated quantum dots, Nano Lett. 7 (2007) 3071–3079.
[17] T.H. Chung, J.K. Hsiao, S.C. Hsu, M. Yao, Y.C. Chen, S.W. Wang, M.Y.P. Kuo, C.S. Yang, D.M. Huang, Iron oxide nanoparticle-induced epidermal growth factor receptor expression in human stem cells for tumor therapy, ACS Nano 5 (2011) 9807–9816.
[18] T. Kim, E. Momin, J. Choi, K. Yuan, H. Zaidi, J. Kim, M. Park, N. Lee, M.T. McMahon, A. Quinones-Hinojosa, J.W.M. Bulte, T. Hyeon, A.A. Gilad, Mesoporous silica-coated hollow manganese oxide nanoparticles as positive T-1 contrast agents for labeling and MRI tracking of adipose-derived mesenchyrnal stem cells, J. Am. Chem. Soc. 133 (2011) 2955–2961.

[19] F. Wang, R. Deng, J. Wang, Q. Wang, Y. Han, H. Zhu, X. Chen, X. Liu, Tuning upconversion through energy migration in core-shell nanoparticles, Nat. Mater. 10 (2011) 968–973.
[20] J. Zhou, Z. Liu, F. Li, Upconversion nanophosphors for small-animal imaging, Chem. Soc. Rev. 41 (2012) 1323–1349.
[21] J. Liu, Y. Liu, Q. Liu, C. Li, L. Sun, F. Li, Iridium(III) complex-coated nanosystem for ratiometric upconversion luminescence bioimaging of cyanide anions, J. Am. Chem. Soc. 133 (2011) 15276–15279.
[22] M. Nyk, R. Kumar, T.Y. Ohulchanskyy, E.J. Bergey, P.N. Prasad, High contrast in vitro and in vivo photoluminescence bioimaging using near infrared to near infrared up-conversion in TM^{3+} and Yb^{3+} doped fluoride nanophosphors, Nano Lett. 8 (2008) 3834–3838.
[23] L.Y. Wang, R.X. Yan, Z.Y. Hao, L. Wang, J.H. Zeng, J. Bao, X. Wang, Q. Peng, Y.D. Li, Fluorescence resonant energy transfer biosensor based on upconversion-luminescent nanoparticles, Angew. Chem. Int. E.d. 44 (2005) 6054–6057.
[24] H.S. Qian, H.C. Guo, P.C.-L. Ho, R. Mahendran, Y. Zhang, Mesoporous-silica-coated up-conversion fluorescent nanoparticles for photodynamic therapy, Small 5 (2009) 2285–2290.
[25] R. Deng, X. Xie, M. Vendrell, Y.-T. Chang, X. Liu, Intracellular glutathione detection using MnO_2-nanosheet-modified upconversion nanoparticles, J. Am. Chem. Soc. 133 (2011) 20168–20171.
[26] Y. Yang, Q. Shao, R. Deng, C. Wang, X. Teng, K. Cheng, Z. Cheng, L. Huang, Z. Liu, X. Liu, B. Xing, In vitro and In vivo uncaging and bioluminescence imaging by using photocaged upconversion nanoparticles, Angew. Chem. Int. E.d. 51 (2012) 3125–3129.
[27] L. Cheng, K. Yang, S. Zhang, M. Shao, S. Lee, Z. Liu, Highly-sensitive multiplexed in vivo imaging using PEGylated upconversion nanoparticles, Nano Res. 3 (2010) 722–732.
[28] C. Wang, H. Tao, L. Cheng, Z. Liu, Near-infrared light induced in vivo photodynamic therapy of cancer based on upconversion nanoparticles, Biomaterials 32 (2011) 6145–6154.
[29] H. Xu, L. Cheng, C. Wang, X. Ma, Y. Li, Z. Liu, Polymer encapsulated upconversion nanoparticle/iron oxide nanocomposites for multimodal imaging and magnetic targeted drug delivery, Biomaterials 32 (2011) 9364–9373.
[30] L. Cheng, K. Yang, Y. Li, J. Chen, C. Wang, M. Shao, S.-T. Lee, Z. Liu, Facile preparation of multifunctional upconversion nanoprobes for multimodal imaging and dual-targeted photothermal therapy, Angew. Chem. Int. E.d. 50 (2011) 7385–7390.
[31] Q. Liu, Y. Sun, T. Yang, W. Feng, C. Li, F. Li, Sub-10 nm hexagonal lanthanide-doped NaLuF4 upconversion nanocrystals for sensitive bioimaging in vivo, J. Am. Chem. Soc. 133 (2011) 17122–17125.
[32] S. Zeng, M. Tsang, C. Chan, K. Wong, J. Hao, PEG modified $BaGdF_5$:Yb/Er nanoprobes for multi-modal upconversion fluorescent, in vivo X-ray computed tomography and biomagnetic imaging, Bioanalysis 33 (2012) 9232–9238.
[33] S. Zeng, H. Wang, W. Lu, Z. Yi, L. Rao, H. Liu, J. Hao, Dual-modal upconversion fluorescent/X-ray imaging using ligand-free hexagonal phase NaLuF 4: Gd/Yb/Er nanorods for blood vessel visualization, Bioanalysis 35 (2014) 2934–2941.
[34] S. Zeng, Z. Yi, W. Lu, C. Qian, H. Wang, L. Rao, T. Zeng, H. Liu, H. Liu, B. Fei, Simultaneous realization of phase/size manipulation, upconversion luminescence enhancement, and blood vessel imaging in multifunctional nanoprobes through transition metal Mn^{2+} doping, Adv. Funct. Mater. 24 (2014) 4051–4059.
[35] Z. Yi, X. Li, Z. Xue, X. Liang, W. Lu, H. Peng, H. Liu, S. Zeng, J. Hao, Remarkable NIR enhancement of multifunctional nanoprobes for in vivo trimodal bioimaging and upconversion optical/T2-weighted MRI-guided small tumor diagnosis, Adv. Funct. Mater. 25 (2015) 7119–7129.
[36] X. Hu, J. Zhu, X. Li, X. Zhang, Q. Meng, L. Yuan, J. Zhang, X. Fu, X. Duan, H. Chen, Dextran-coated fluorapatite crystals doped with Yb 3+/Ho 3+ for labeling and tracking chondrogenic differentiation of bone marrow mesenchymal stem cells in vitro and in vivo, Biomaterials 52 (2015) 441–451.
[37] C. Wang, L. Cheng, H. Xu, Z. Liu, Towards whole-body imaging at the single cell level using ultra-sensitive stem cell labeling with oligo-arginine modified upconversion nanoparticles, Biomaterials 33 (2012) 4872–4881.
[38] N.M. Idris, Z. Li, L. Ye, E.K.W. Sim, R. Mahendran, P.C.-L. Ho, Y. Zhang, Tracking transplanted cells in live animal using upconversion fluorescent nanoparticles, Biomaterials 30 (2009) 5104–5113.
[39] F. Wang, X. Liu, Recent advances in the chemistry of lanthanide-doped upconversion nanocrystals, Chem. Soc. Rev. 38 (2009) 976–989.
[40] A. Verma, F. Stellacci, Effect of surface properties on nanoparticle–cell interactions, Small 6 (2010) 12–21.
[41] Z.G. Qu, X.C. He, M. Lin, B.Y. Sha, X.H. Shi, T.J. Lu, F. Xu, Advances in the understanding of nanomaterial-biomembrane interactions and their mathematical and numerical modeling, Nanomedicine 8 (2013) 995–1011.
[42] B.D. Chithrani, A.A. Ghazani, W.C. Chan, Determining the size and shape dependence of gold nanoparticle uptake into mammalian cells, Nano Lett. 6 (2006) 662–668.
[43] R.A. Jalil, Y. Zhang, Biocompatibility of silica coated $NaYF_4$ upconversion fluorescent nanocrystals, Biomaterials 29 (2008) 4122–4128.
[44] J. Zhang, F. Liu, T. Li, X. He, Z. Wang, Surface charge effect on the cellular interaction and cytotoxicity of NaYF4:Yb^{3+}, Er^{3+}@SiO2 nanoparticles, RSC Adv. 5 (2015) 7773–7780.
[45] J. Ouyang, D. Yin, K. Song, C. Wang, B. Liu, M. Wu, Recent advances of $NaLuF_4$-based upconversion nanocrystals, J. Nanosci. Nanotechnol. 15 (2015) 31–40.
[46] M. You, J. Zhong, Y. Hong, Z. Duan, M. Lin, F. Xu, Inkjet printing of upconversion nanoparticles for anti-counterfeit applications, Nanoscale 7 (2015) 4423–4431.
[47] A. Alhadlaq, J.J. Mao, Mesenchymal stem cells: Isolation and therapeutics, Stem Cells Dev. 13 (2004) 436–448.
[48] J. Juan, L. Cheng, M. Shi, Z. Liu, X. Mao, Poly-(allylamine hydrochloride)-coated but not poly (acrylic acid)-coated upconversion nanoparticles induce autophagy and apoptosis in human blood cancer cells, J. Mater. Chem. B 3 (2015) 5769–5776.
[49] Y. Zhu, W. Meng, X. Li, H. Gao, N. Hanagata, Design of mesoporous silica/cytosine−phosphodiester−guanine oligodeoxynucleotide complexes to enhance delivery efficiency, J. Phys. Chem. C 115 (2011) 447–452.
[50] J. Li, H. Jiang, Z. Yu, H. Xia, G. Zou, Q. Zhang, Y. Yu, Multifunctional uniform core-shell Fe_3O_4@$mSiO_2$ mesoporous nanoparticles for bimodal imaging and photothermal therapy, Chem-Asian J. 8 (2013) 385.
[51] A.M. Alkilany, C.J. Murphy, Toxicity and cellular uptake of gold nanoparticles: what we have learned so far?, J Nanopart. Res. 12 (2010) 2313.
[52] S.H. Wang, C.W. Lee, K.C. Shen, F.G. Tseng, P.K. Wei, Dose dependent distribution and aggregation of gold nanoparticles within human lung adeno-carcinoma cells, Rsc Adv. 5 (2015) 98309–98317.
[53] Y. Sun, W. Feng, P. Yang, C. Huang, F. Li, The biosafety of lanthanide upconversion nanomaterials, Chem. Soc. Rev. 44 (2015) 1509–1525.
[54] T. Moriguchi, K. Yano, S. Nakagawa, F. Kaji, Elucidation of adsorption mechanism of bone-staining agent alizarin red S on hydroxyapatite by FT-IR microspectroscopy, J. colloid interf. sci. 260 (2003) 19–25.
[55] R. Sakhtianchi, R.F. Minchin, K.B. Lee, A.M. Alkilany, V. Serpooshan, M. Mahmoudi, Exocytosis of nanoparticles from cells: role in cellular retention and toxicity, Adv. Colloid Interfaces 201 (2013) 18–29.
[56] L. Zhao, A. Kutikov, J. Shen, C. Duan, J. Song, G. Han, Stem cell labeling using polyethylenimine conjugated (alpha-$NaYbF_4$:Tm^{3+})/CaF_2 upconversion nanoparticles, Theranostics 3 (2013) 249–257.
[57] N.D. Sonawane, F.C. Szoka, A. Verkman, Chloride accumulation and swelling in endosomes enhances DNA transfer by polyamine-DNA polyplexes, J. Biol. Chem. 278 (2003) 44826–44831.
[58] I. Stayton, J. Winiarz, K. Shannon, Y. Ma, Study of uptake and loss of silica nanoparticles in living human lung epithelial cells at single cell level, Anal. Bioanal. Chem. 394 (2009) 1595–1608.
[59] M.S. Cartiera, K.M. Johnson, V. Rajendran, M.J. Caplan, W.M. Saltzman, The uptake and intracellular fate of PLGA nanoparticles in epithelial cells, Biomaterials 30 (2009) 2790–2798.